Electronic Supplementary Information (ESI)

Electro-activation Driven Self-Dispersion of PdCuAg Nanoparticles for High-Performance Formic Acid Oxidation

Jianyi Zhang,[a] Yiting Song,[a] Jialin Cui,[a] Shiyue Xing, [a] Zhongliang Liu, [a] Yulv Yu, [c]*Jie Sun,[c] Tianrui Xue, [a] Dongjie Qin, [a] Zhenxue Liu, [c] Huihui Li* [a] and Chunzhong Li* [a b]

a. Key Laboratory for Ultrafine Materials of Ministry of Education, School of Chemical Engineering,East China University of Science and Technology,Shanghai 200237, China. E-mail: huihuili@ecust.edu.cn; czli@ecust.edu.cn

b. Shanghai Engineering Research Center of Hierarchical Nanomaterials, School of Materials Science and Engineering, East China University of Science and Technology, Shanghai 200237, China.

c. Chambroad Institute, Shandong, 256500，China.

Experimental

Materials and chemicals

Potassium tetrachloropalladate (K_2PdCl_4, 98%), tungsten hexacarbonyl ($W(CO)_6$, ≥97%), cupric chloride dihydrate ($CuCl_2·2H_2O$), ascorbic acid (AA, ≥99%), formic acid (CH_2O_2, ≥99%), acetic acid ($C_2H_4O_2$, ≥99.7%), N,N-dimethylformamide (DMF, ≥99.9%), and polyvinylpyrrolidone (PVP, MW = 58000) were purchased from Aladdin. Ethylene glycol ($C_2H_6O_2$, ≥99%) and silver nitrate ($AgNO_3$, 99.7%) were purchased from Macklin. 2-propanol (C_3H_8O, HPLC, 99.9%) was purchased from Honeywell. Carbon black (Vulcan XC-72) was purchased from Cabot. Ethanol (C_2H_6O, ≥99.7%) and perchloric acid ($HClO_4$, 70~72 wt. %) were purchased from General-Reagent. Perfluorinated resin solution containing Nafion^{TM} 1100W (5 wt. % in lower aliphatic alcohols and water, contains 15-20% water) was purchased from Sigma-Aldrich. Commercial Pd/C catalyst (10 wt%, 2-5 nm Pd nanoparticles) was obtained from Johnson Matthey. All the chemicals were used as received without further purification. All the experimental water used was deionized water(18.25 MΩ cm).

Preparation of PdCuAg NCFs, PdAg NCFs, PdCu NCFs and Pd NCFs

In a typical synthesis of PdCuAg NCFs, K_2PdCl_4 (10 mg, 0.0306 mmol), $W(CO)_6$ (50 mg, 0.1420 mmol), and $CuCl_2·2H_2O$ (12 mg, 0.0704 mmol) were initially introduced into a round-bottom flask (25 mL), followed by the addition of DMF (8 mL) and acetic acid (2 mL) as the solvent system. The mixture was ultrasonicated to ensure complete homogenization and subsequently heated in an oil bath at 140 °C for 2 h. Upon completion of the reaction, the obtained intermediate product was collected by centrifugation at 8000 rpm for 5 min after being washed three times with deionized water and ethanol. The resulting intermediate was then redispersed in ethylene glycol (10 mL), followed by the successive addition of $AgNO_3$ (1.5 mg, 0.0088 mmol), PVP (25 mg), and AA (25 mg). The mixture was ultrasonicated to form a homogeneous solution and subsequently heated in an oil bath at 130 °C for 1 h. The as-synthesized PdCuAg NCFs were washed three times with deionized water and ethanol, and centrifuged at 8000 rpm for 5 min to obtain the final product. Finally, the products were dispersed in 2-propanol (10 mL) for further use.

In a typical synthesis of PdAg NCFs, K_2PdCl_4 (10 mg, 0.0306 mmol) and $W(CO)_6$ (50 mg, 0.1420 mmol) were initially introduced into a round-bottom flask (25 mL), followed by the addition of DMF (8 mL) and acetic acid (2 mL) as the solvent system. The mixture was ultrasonicated to ensure complete homogenization and subsequently heated in an oil bath at 140 °C for 2 h. Upon completion of the reaction, the obtained intermediate product was collected by centrifugation at

8000 rpm for 5 min after being washed three times with deionized water and ethanol. The resulting intermediate was then redispersed in ethylene glycol (10 mL), followed by the successive addition of $AgNO_3$ (1.5 mg, 0.0088 mmol), PVP (25 mg), and AA (25 mg). The mixture was ultrasonicated to form a homogeneous solution and subsequently heated in an oil bath at 130 °C for 1 h. The as-synthesized PdAg NCFs were washed three times with deionized water and ethanol, and centrifuged at 8000 rpm for 5 min to obtain the final product. Finally, the products were dispersed in 2-propanol (10 mL) for further use.

In a typical synthesis of PdCu NCFs, K_2PdCl_4 (10 mg, 0.0306 mmol), $W(CO)_6$ (50 mg, 0.1420 mmol), and $CuCl_2·2H_2O$ (12 mg, 0.0704 mmol) were initially introduced into a round-bottom flask (25 mL), followed by the addition of DMF (8 mL) and acetic acid (2 mL) as the solvent system. The mixture was ultrasonicated to ensure complete homogenization and subsequently heated in an oil bath at 140 °C for 2 h. Upon completion of the reaction, the obtained intermediate product was collected by centrifugation at 8000 rpm for 5 min after being washed three times with deionized water and ethanol. Finally, the products were dispersed in 2-propanol (10 mL) for further use.

In a typical synthesis of Pd NCFs, K_2PdCl_4 (10 mg, 0.0306 mmol) and $W(CO)_6$ (50 mg, 0.1420 mmol) were initially introduced into a round-bottom flask (25 mL), followed by the addition of DMF (8 mL) and acetic acid (2 mL) as the solvent system. The mixture was ultrasonicated to ensure complete homogenization and subsequently heated in an oil bath at 140 °C for 2 h. Upon completion of the reaction, the obtained intermediate product was collected by centrifugation at 8000 rpm for 5 min after being washed three times with deionized water and ethanol. Finally, the products were dispersed in 2-propanol (10 mL) for further use.

Characterizations

The morphological and structural features of the catalysts were examined using transmission electron microscopy (TEM), high-angle annular dark-field scanning transmission electron microscopy (HAADF-STEM), and energy-dispersive X-ray spectroscopy (EDS) performed on an FEI Talos F200X microscope to analyze the nanostructure, morphology, and elemental distribution. The crystalline structure was characterized by X-ray diffraction (XRD) using a Bruker D8 Advance diffractometer (Bruker, Germany) with Cu Kα radiation ($\lambda = 0.15406$ nm). X-ray photoelectron spectroscopy (XPS) measurements were carried out on a Kratos AXIS Supra+ spectrometer (Kratos, Japan) equipped with a monochromatic Al Kα X-ray source. The elemental composition and the Pd loading on the glassy carbon were determined using an Agilent 5800 inductively coupled plasma optical emission spectrometer (ICP-OES, Agilent, USA). Zeta potential measurements were conducted using a Zetasizer ZEN3600 (Malvern Instruments Limited, UK).

Electrochemical Measurements

Prior to the electrochemical measurements, homogeneous catalyst ink was prepared by ultrasonic dispersion. Specifically, the catalyst 2-propanol suspension (990 uL), a 5 wt% Nafion solution (10 uL), and XC-72 carbon powder (2 mg) were mixed and ultrasonicated for approximately 30 min to obtain a uniform suspension. The concentration of the catalyst ink was determined by ICP-OES. For electrode preparation, the catalyst ink (5 uL) was deposited onto a clean glassy carbon (GC, diameter 3 mm) and dried at room temperature to serve as the working electrode. A saturated Ag/AgCl electrode and a graphite rod were used as the reference and counter electrodes, respectively. The Pd loading on the GC was controlled at 10 μg cm^{-2}.

All electrochemical measurements were carried out on a CHI760E electrochemical workstation (CH Instruments, Shanghai, China) using a conventional three-electrode configuration at room temperature. All recorded potentials were converted to the reversible hydrogen electrode (RHE) scale according to the Nernst equation, and all values reported herein are referenced to RHE. Cyclic voltammetry (CV) measurements were performed in N_2-saturated 0.1 M $HClO_4$ solution. Prior to testing, high-purity nitrogen was purged into the electrolyte for 20 min to remove dissolved oxygen. Electrochemical activation was carried out in N_2-saturated 0.1 M $HClO_4$ by cycling the working electrode between 0 and 1.2 V vs. RHE at 250 mV s^{-1}. The Pd loading was controlled at 10 μg cm^{-2}. The activation cycle number was screened to evaluate the evolution of FAOR activity and ECSA. The selected activation condition provides sufficient Cu dissolution and structural reconstruction while avoiding unnecessary over-cycling. CV measurements were subsequently conducted in the same potential range at a scan rate of 50 mV s^{-1}. The electrochemically active surface area (ECSA) of Pd was calculated using the equation:

$$ECSA = \frac{Q_{PdO}}{C \times m_{Pd}}$$

where Q_{PdO} represents the charge associated with PdO reduction in the CV curve, C is the charge required for monolayer adsorption of hydrogen on a Pd (0.405 mC cm^{-2}) surface, and m_{Pd} denotes the Pd loading on the GC. The formic acid oxidation reaction (FAOR) was performed in a mixed electrolyte containing 0.1 M $HClO_4$ and 0.5 M HCOOH, within a potential range of 0-1.2 V (vs. RHE) at a scan rate of 50 mV s^{-1}. The chronoamperometry (CA) measurements for FAOR stability were conducted at a fixed potential of 0.55 V (vs. RHE) in the same electrolyte. Linear sweep voltammetry (LSV) was conducted to record polarization curves for the FAOR in N_2-saturated 0.1 M $HClO_4$ and 0.5 M HCOOH at a scan rate of 5 mV s^{-1}.

CO stripping measurements were conducted in N_2-saturated 0.1 M $HClO_4$. CO was first adsorbed onto the catalyst surface by bubbling high-purity CO through the electrolyte for 20 min while holding the electrode at 0.1 V vs. RHE. Excess dissolved CO was then removed by purging with N_2 for 20 min. The stripping voltammograms were subsequently recorded between 0 and 1.2 V vs. RHE at a scan rate of 50 mV s^{-1}. Accelerated durability tests (ADT) were performed in 0.1 M $HClO_4$ + 0.5 M HCOOH by continuous potential cycling between 0.05 and 0.7 V vs. RHE at a scan rate of 200 mV s^{-1} for up to 10000 cycles.

The calculation method of d-band centers:

The d-band centers of all catalysts were calculated from the following equation based on the valence band spectra:

$$d-band\ center=-\frac{\int_{-2eV}^{10eV}[binding\ energy(E)intensity(E)]dE}{\int_{-2eV}^{10eV}intensity(E)dE}$$

The calculation of α and j_0:

The Tafel slopes of all studied FAOR electrocatalysts were determined from the corresponding Tafel plots using the following equation:

$$\eta=blogj+a=\frac{2.3RT}{\alpha nF}logj-\frac{2.3RT}{\alpha nF}logj_0$$

where R is the gas constant, T is the absolute temperature, α is the charge-transfer coefficient, F is the Faraday constant, and j_0 (mA cm^{-2}) is the exchange current density.

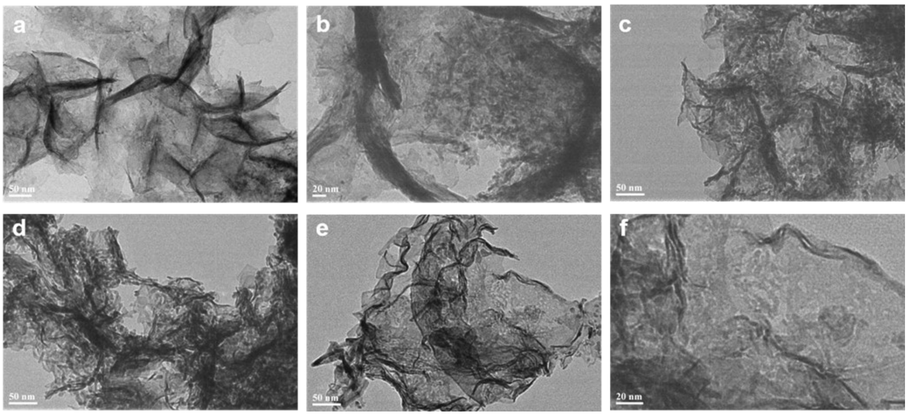

Fig. S1. TEM images of (a, b) Pd NCFs, (c, d) PdCu NCFs, and (e, f) PdAg NCFs.

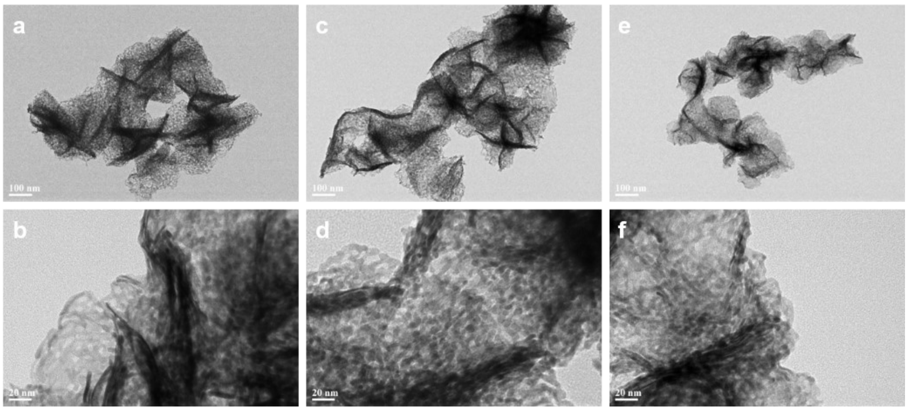

Fig. S2. TEM images of PdCuAg samples with different compositions. (a, b) $Pd_{48}Cu_{47}Ag_5$ with Pd:Cu approximately 1:1. (c, d) $Pd_{63}Cu_{30}Ag_7$ with Pd:Cu approximately 2:1. (e, f) $Pd_{70}Cu_{24}Ag_6$ with Pd:Cu approximately 3:1.

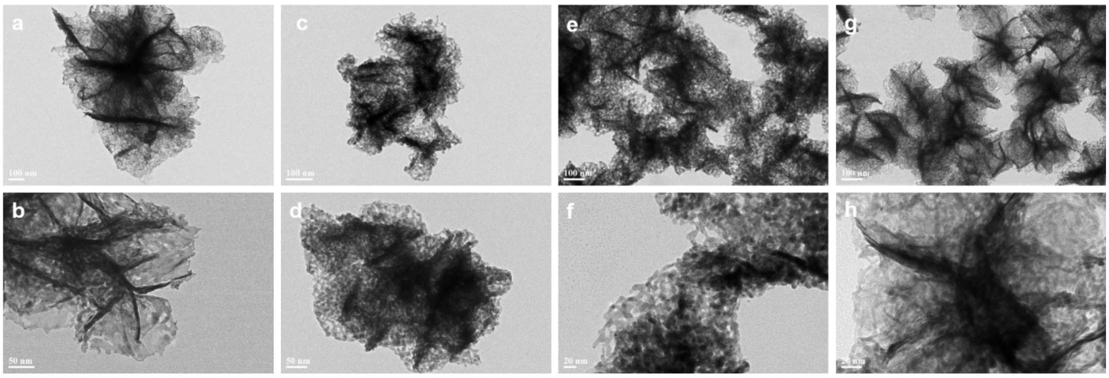

Fig. S3. TEM images of additional PdCuAg composition-control samples. (a, b) $Pd_{69}Cu_{27}Ag_4$. (c, d) $Pd_{43}Cu_{49}Ag_8$. (e, f) $Pd_{51}Cu_{37}Ag_{12}$. (g, h) $Pd_{58}Cu_{39}Ag_3$.

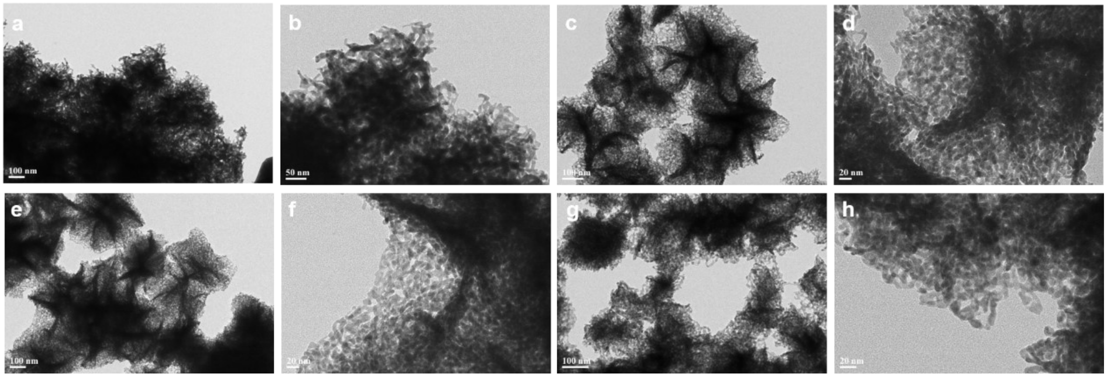

Fig. S4. TEM images of PdCuAg NCFs synthesized with different $W(CO)_6$ dosages: (a, b) 25 mg, (c, d) 75 mg, (e, f) 100 mg, and (g, h) 125 mg.

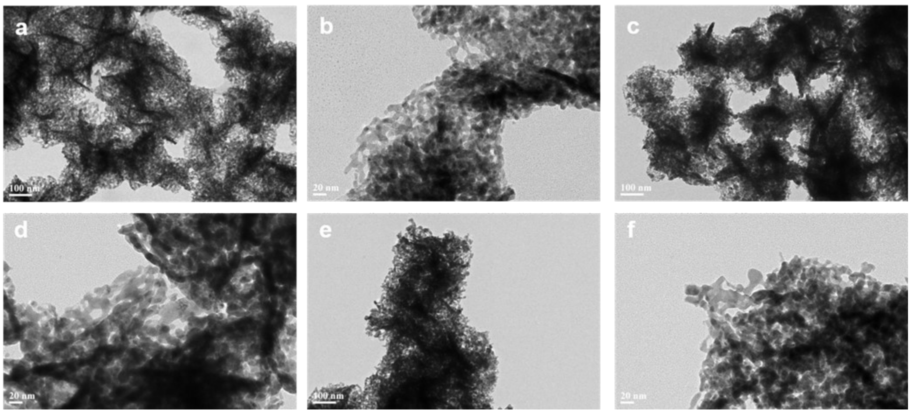

Fig. S5. TEM images of PdCuAg NCFs synthesized with different $AgNO_3$ dosages: (a, b) 3 mg, (c, d) 4.5 mg, and (e, f) 6 mg.

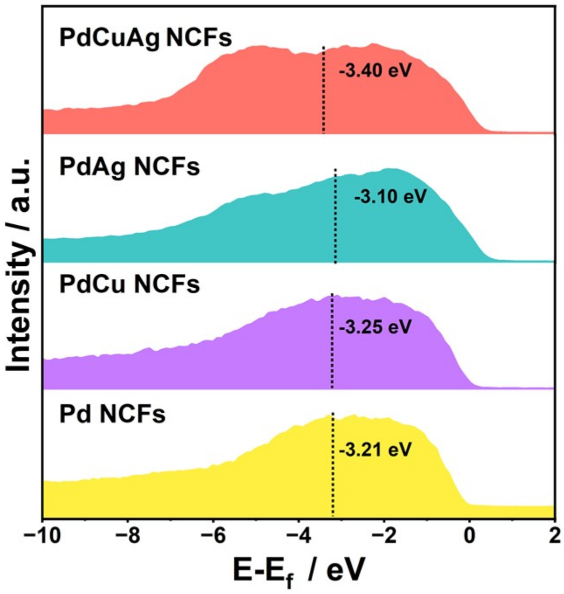

Fig. S6. D-band center comparison of PdCuAg NCFs and the reference samples (PdAg NCFs, PdCu NCFs, and Pd NCFs).

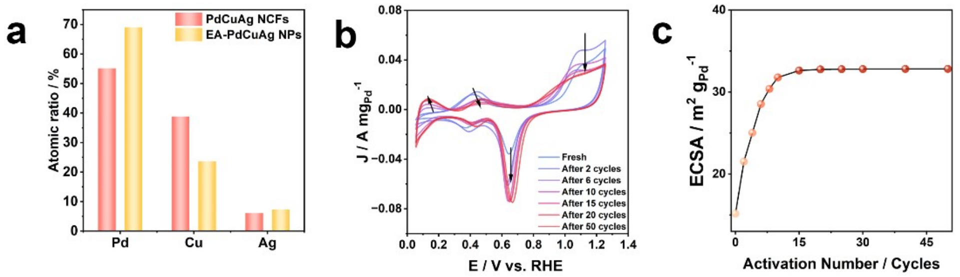

Fig. S7. Electrochemical performance of PdCuAg NCFs during the potential activation cycling process.: (a) Comparison of the atomic ratios of Pd, Cu, and Ag in PdCuAg NCFs and EA-PdCuAg NPs. (b) CV curves of PdCuAg NCFs recorded at different activation cycles. (c) Evolution of the ECSA of PdCuAg NCFs as a function of activation cycle number.

Note: The activation CV curves show a gradual decrease of the Cu oxidation feature, while no clear cathodic peak or shoulder corresponding to Cu^{2+}/Cu or Cu^{+}/Cu reduction has been observed. Together with the decrease of Cu content from 38.82% to 23.60% by ICP-OES, these results indicate that electrochemical activation is dominated by net Cu dissolution rather than substantial Cu redeposition.

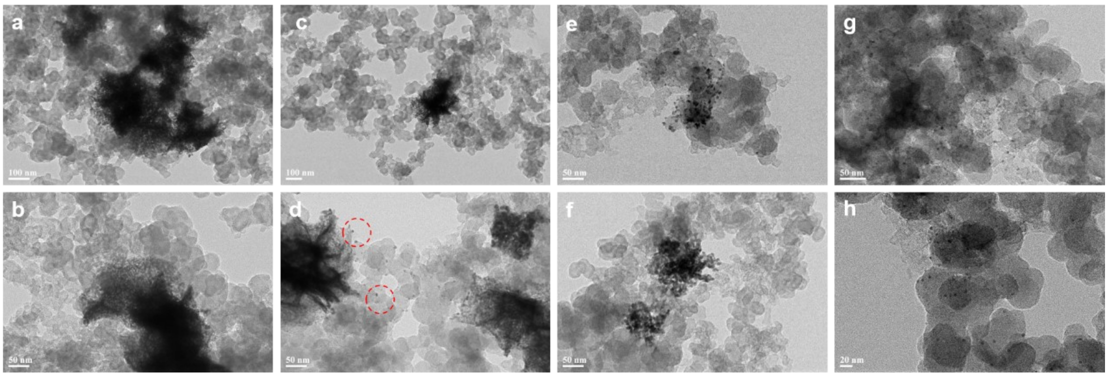

Fig. S8. Time-dependent ex situ TEM images of PdCuAg catalysts after different electrochemical activation stages. (a, b) 5 activation cycles. (c, d) 10 activation cycles. (e, f) 15 activation cycles. (g, h) 20 activation cycles.

Note: The time-dependent ex situ TEM images show a gradual morphology evolution from nanosheet-assembled nanoflowers to dispersed nanoparticles during electrochemical activation. This observation supports the proposed Cu-dissolution-driven self-dispersion process.

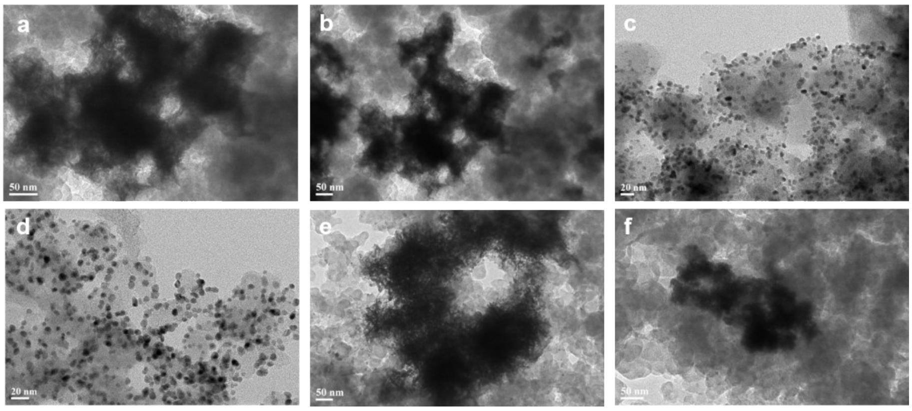

Fig. S9. TEM images of (a,b) EA-Pd, (c,d) EA-PdCu, and (e,f) EA-PdAg.

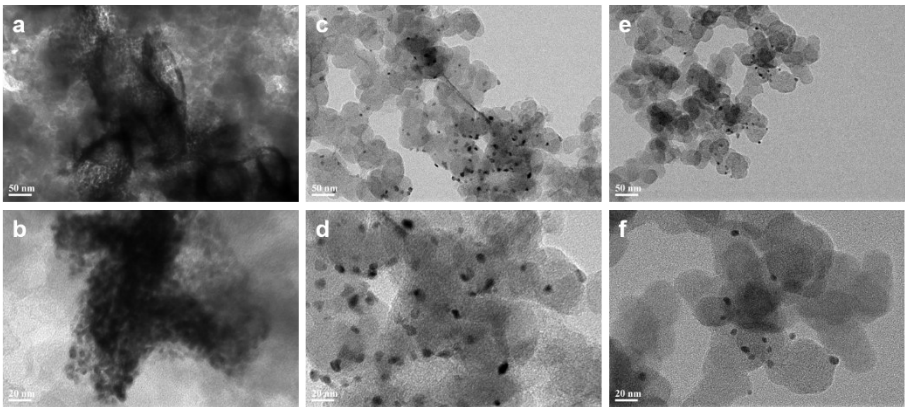

Fig. S10. TEM images of PdCuAg samples with different Pd:Cu ratios after 50 electrochemical activation cycles. (a, b) $Pd_{48}Cu_{47}Ag_5$ with Pd:Cu approximately 1:1. (c, d) $Pd_{63}Cu_{30}Ag_7$ with Pd:Cu approximately 2:1. (e, f) $Pd_{70}Cu_{24}Ag_6$ with Pd:Cu approximately 3:1.

Note: The Cu-content-dependent comparison indicates that Cu dissolution is closely related to the reconstruction behavior. Excessive Cu content helps maintain the original framework, whereas lower Cu content favors structural fragmentation and nanoparticle redistribution during activation.

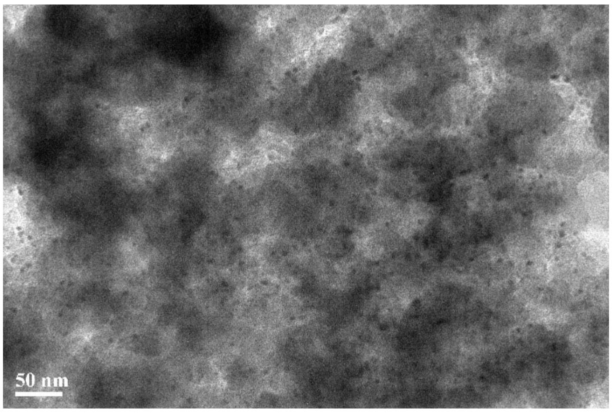

Fig. S11. Preliminary scalability evaluation of the electrochemical self-dispersion strategy. TEM images of the catalyst after activation on a glassy carbon electrode with a diameter of 5 mm.

Note: The self-dispersed nanoparticle morphology has been observed under larger-electrode conditions, supporting the reproducibility and preliminary scalability of the electrochemical activation strategy.

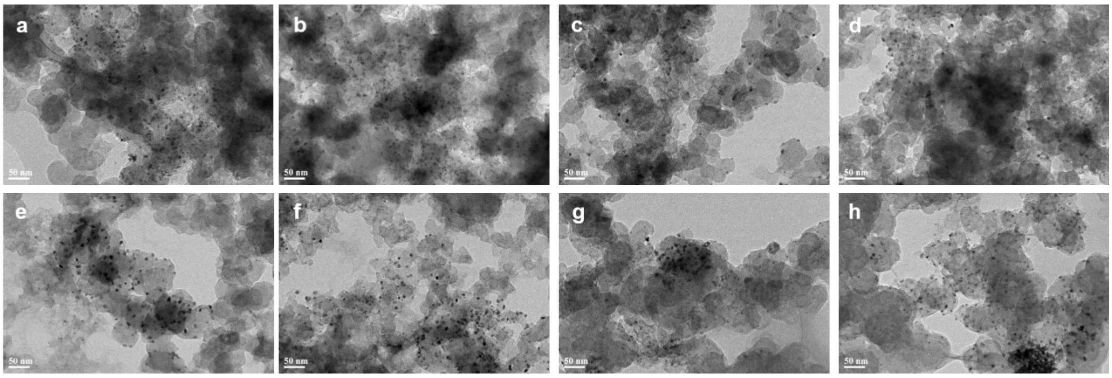

Fig. S12. TEM images of EA-PdCuAg NPs, synthesized with different $W(CO)_6$ dosages: (a, b) 25 mg, (c, d) 75 mg, (e, f) 100 mg, and (g, h) 125 mg.

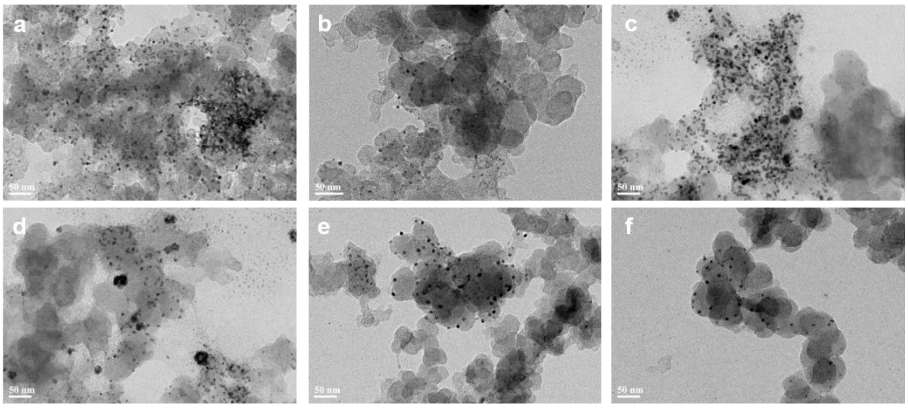

Fig. S13. TEM images of EA-PdCuAg NPs, synthesized with different $AgNO_3$ dosages: (a, b) 3 mg, (c, d) 4.5 mg, and (e, f) 6 mg.

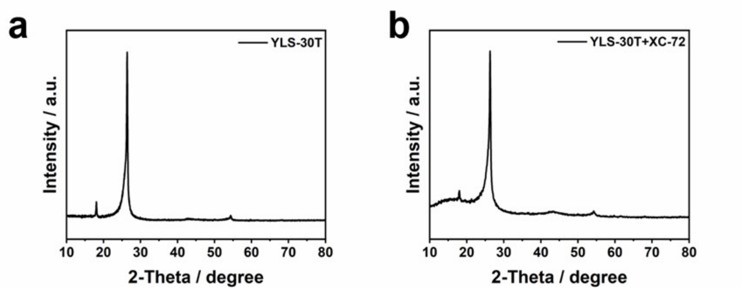

Fig. S14. XRD patterns of (a) pristine YLS-30T carbon paper and (b) YLS-30T carbon paper loaded with XC-72 carbon.

Note: A broad diffraction feature located in the low-angle region (approximately 10-20°) is observed only after the introduction of XC-72 carbon, indicating that this signal originates from the amorphous carbon structure of XC-72 rather than from Pd-, Cu-, or Ag-containing crystalline phases.

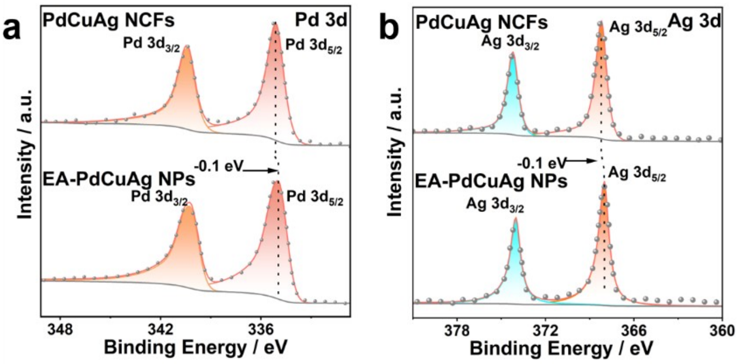

Fig. S15. High-resolution XPS spectra of PdCuAg NCFs and EA-PdCuAg NPs: (a) Pd 3d, (b) Ag 3d.

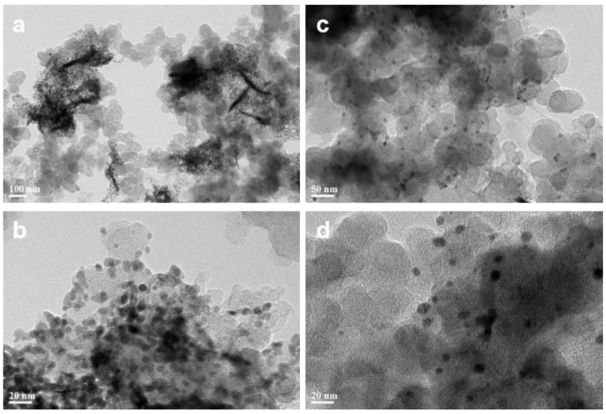

Fig. S16. Morphological characterization of the directly synthesized PdCuAg/XC-72 control sample. (a, b) TEM images of PdCuAg/XC-72 prepared by directly introducing XC-72 during the initial synthesis stage. (c, d) TEM images of the EA-PdCuAg/XC-72 samples after electrochemical activation.

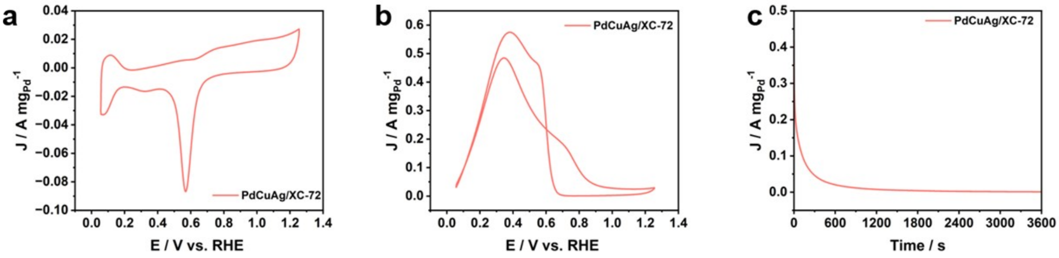

Fig. S17. Electrochemical performance of the directly synthesized PdCuAg/XC-72 control sample. (a) CV curves. (b) FAOR polarization curves. (c) CA durability curves.

Note: To clarify whether direct carbon-supported synthesis can reproduce the performance of EA-PdCuAg NPs, a PdCuAg/XC-72 control sample was prepared by introducing XC-72 during the initial synthesis stage. TEM images show that the PdCuAg species are deposited on XC-72 carbon aggregates with an inhomogeneous distribution, rather than forming well-defined PdCuAg NCFs. After electrochemical activation, small nanoparticles can be observed, but EA-PdCuAg/XC-72 remain unevenly distributed on the carbon support and do not form the uniform self-dispersed nanoparticle morphology observed for EA-PdCuAg NPs.

Electrochemical measurements further show that EA-PdCuAg/XC-72 exhibits much lower FAOR activity, with a MA of only 0.49 A mg_{Pd}^{-1}. The CA test also shows poorer current retention than EA-PdCuAg NPs. These results indicate that simply introducing carbon support during synthesis cannot reproduce the optimized morphology, active-site exposure, or durability of EA-PdCuAg NPs. Therefore, the superior FAOR performance of EA-PdCuAg NPs originates from the electro-activation-driven reconstruction and self-dispersion of the PdCuAg NCF precursor.

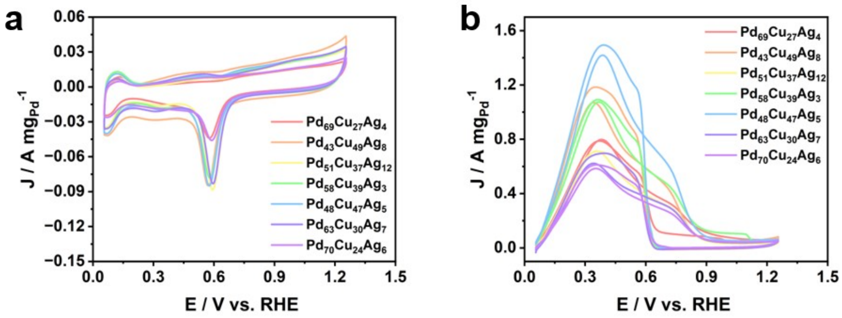

Fig. S18. Electrochemical comparison of PdCuAg samples with different compositions. (a) CV curves in 0.1 M $HClO_4$. (b) FAOR polarization curves in 0.1 M $HClO_4$ + 0.5 M HCOOH.

Note: The composition-dependent comparison shows that changing Pd, Cu, or Ag content substantially affects both morphology and FAOR performance. The optimized EA-PdCuAg NPs exhibit the highest MA among these composition-control samples, indicating that the high activity arises from a balanced ternary composition together with activation-induced self-dispersion.

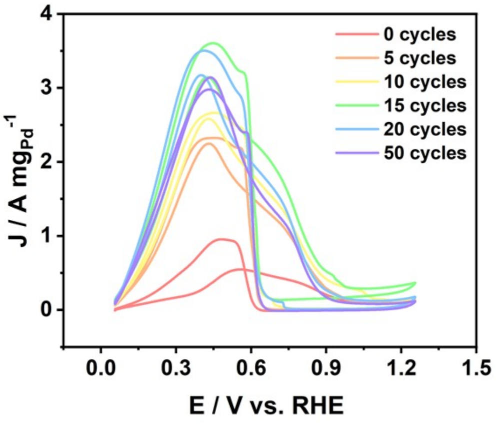

Fig. S19. FAOR polarization curves of PdCuAg catalysts after different electrochemical activation cycle numbers in 0.1 M $HClO_4$ + 0.5 M HCOOH.

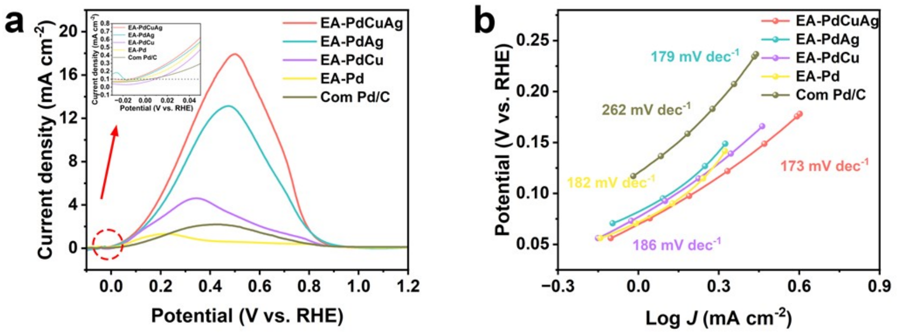

Fig. S20. Kinetic analysis of FAOR on EA-PdCuAg NPs and reference catalysts. (a) LSV curves. (b) Tafel plots.

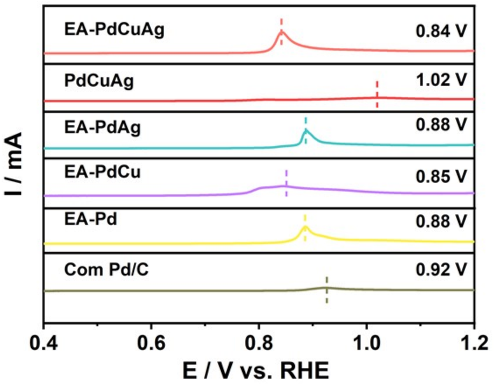

Fig. S21. CO stripping curves of EA-PdCuAg NPs, PdCuAg NCFs, EA-PdAg, EA-PdCu, EA-Pd, and commercial Pd/C.

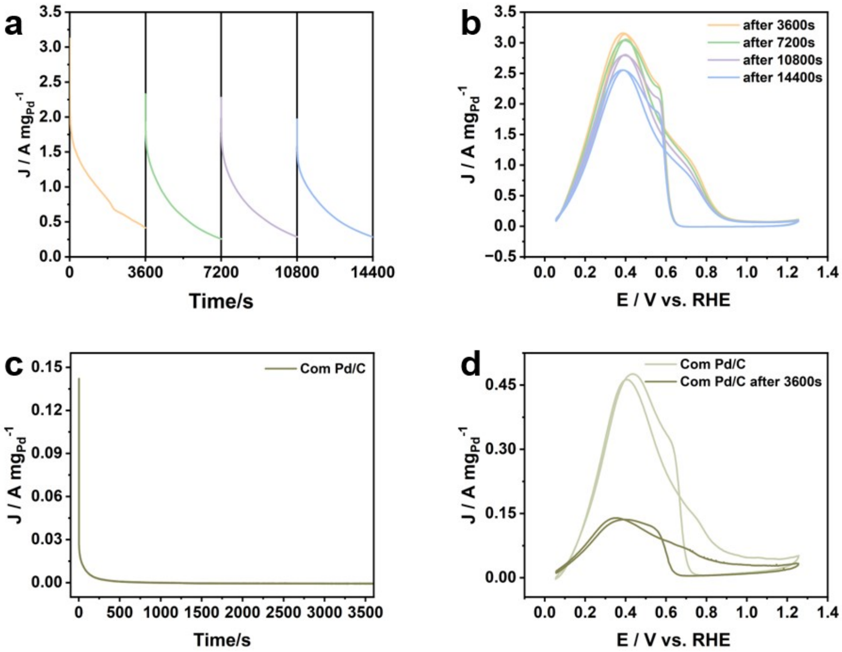

Fig. S22. Extended CA durability evaluation of EA-PdCuAg NPs and commercial Pd/C. (a) 14400s CA curve of EA-PdCuAg NPs at 0.55 V vs. RHE in 0.1 M $HClO_4$ + 0.5 M HCOOH. (b) FAOR polarization curves of EA-PdCuAg NPs collected after each 3600 s CA interval. (c) CA curve of commercial Pd/C under the same electrolyte condition. (d) FAOR polarization curve of commercial Pd/C after 3600 s CA test.

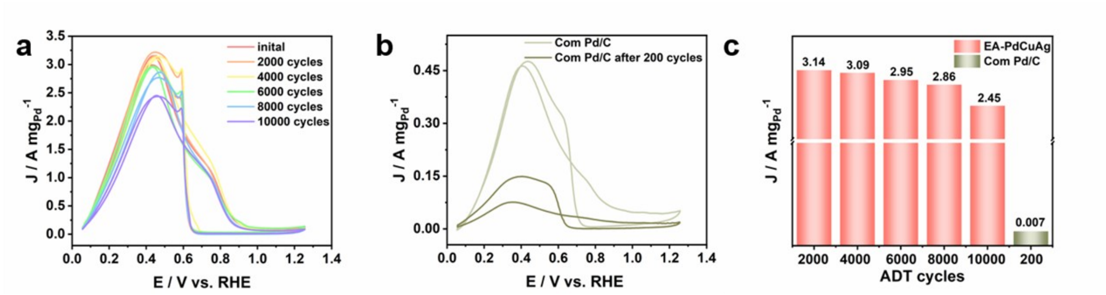

Fig. S23. Accelerated durability test of EA-PdCuAg NPs and commercial Pd/C. (a) FAOR polarization curves of EA-PdCuAg NPs after different ADT cycle numbers. (b) FAOR polarization curves of commercial Pd/C before and after 200 cycles. (c) MA comparison after ADT cycling.

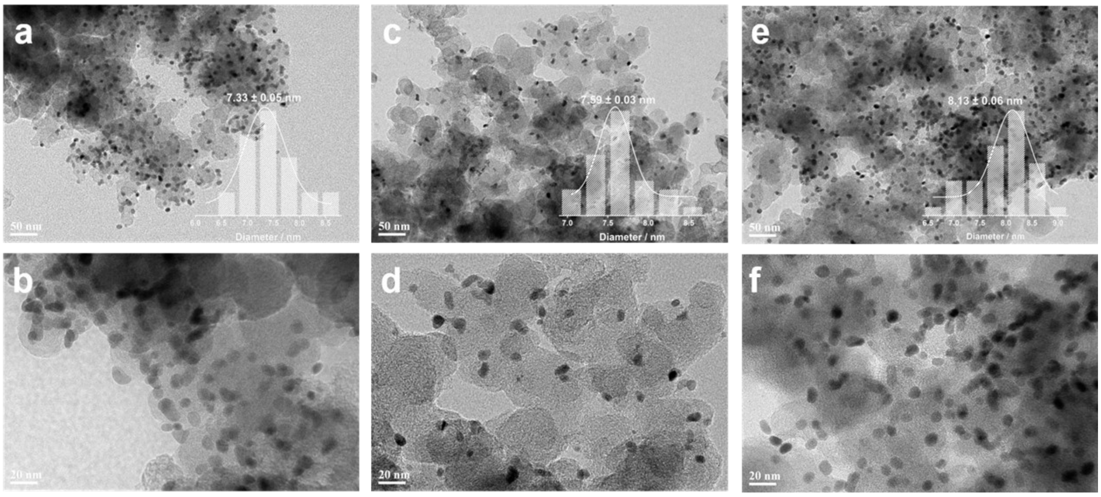

Fig. S24. TEM images of EA-PdCuAg NPs after ADT. (a, b) after 2000 cycles, (c, d) after 4000 cycles, and (e, f) after 10000 cycles. Insets in (a), (c), and (e) show the corresponding particle size distribution histograms.

Note: Post-ADT TEM characterization shows that EA-PdCuAg NPs remain well dispersed on the carbon support without obvious aggregation after prolonged cycling. The average particle size increases only slightly from 7.25 nm initially to 7.33, 7.59, and 8.13 nm after 2,000, 4,000, and 10,000 cycles, respectively, confirming the excellent structural durability of the activation-induced self-dispersed nanoparticles.

Table S1. The compositions of the PdCuAg NCFs, PdAg NCFs, PdCu NCFs, Pd NCFs by ICP-OES.

Sample	Pd (atom %)	Cu (atom %)	Ag (atom %)
PdCuAg NCFs	55.12	38.82	6.06
PdAg NCFs	82.49	—	17.51
PdCu NCFs	40.74	59.26	—
Pd NCFs	100.00	—	—

Table S2. The compositions of the PdCuAg NCFs, EA-PdCuAg NPs, EA-PdAg, EA-PdCu by ICP-OES.

Sample	Pd (atom %)	Cu (atom %)	Ag (atom %)
PdCuAg NCFs	55.12	38.82	6.06
EA-PdCuAg NPs	69.05	23.60	7.35
EA-PdAg	90.28	—	9.72
EA-PdCu	77.45	22.55	—

Note: The ICP-OES results confirm partial Cu dissolution during electrochemical activation and show that residual Cu and Ag remain in the activated PdCuAg nanoparticles.

Table S3. The performance comparison of the EA-PdCuAg NPs catalyst with various Pd-based catalysts toward FAOR.

Sample	Test Condition	Mass Activity (A mg_{Pd}^{-1})	Specific activity (mA cm^{-2})	Reference
EA-PdCuAg NPs	0.1 M $HClO_4$ + 0.5 M FA	3.15	9.57	This work
O-PdBi/C	0.1 M H_2SO_4 + 0.5 M FA	1.02	3.20	[1]
PdNiP-H	0.1 M H_2SO_4 + 0.5 M FA	1.99	1.99	[2]
POM-Pd-20-P01	0.1 M H_2SO_4 + 0.5 M FA	3.34	3.69	[3]
a-PdCu NWs	0.1 M H_2SO_4 + 0.5 M FA	2.93	5.12	[4]
L-Pd/PdWCr	0.1 M H_2SO_4 + 0.5 M FA	2.09	2.34	[5]
P-PdNTA	0.1 M H_2SO_4 + 0.5 M FA	3.64	4.41	[6]
Ordered PdCu	0.1 M H_2SO_4 + 0.5 M FA	0.67	1.88	[7]
$PdFe_3$/rGO	0.1 M H_2SO_4 + 0.5 M FA	0.83	10.52	[8]
Pd_3P PNTs	0.1 M H_2SO_4 + 0.5 M FA	0.36	7.01	[9]
PdIr bimetallene	0.1 M $HClO_4$ + 0.5 M FA	2.70	2.12	[10]
Pd/NiN_4Cl	0.1 M $HClO_4$ + 0.5 M FA	2.26	2.70	[11]
PdSn/WO_3	0.1 M H_2SO_4 + 0.5 M FA	1.60	5.93	[12]
O-PdCu/C	0.5 M H_2SO_4 +0.5 M HCOOH	1.06	2.42	[13]
PdCuCo/C	0.5 M H_2SO_4 +0.5 M HCOOH	2.14	2.15	[14]
SnO_2@Pd NC	0.1 M $HClO_4$ + 0.5 M HCOOH	2.46	-	[15]

Table S4. MA values of PdCuAg samples with different Pd:Cu:Ag ratios.

Sample	Composition-control strategy	MA (A mg_{Pd}^{-1})
$Pd_{69}Cu_{27}Ag_4$	Cu/Ag ratio approximately unchanged	0.80
$Pd_{43}Cu_{49}Ag_8$	Cu/Ag ratio approximately unchanged	1.06
$Pd_{51}Cu_{37}Ag_{12}$	Pd/Cu ratio approximately unchanged	0.71
$Pd_{58}Cu_{39}Ag_3$	Pd/Cu ratio approximately unchanged	1.08
$Pd_{48}Cu_{47}Ag_5$	Pd/Ag ratio approximately unchanged; Pd:Cu approximately 1:1	1.42
$Pd_{63}Cu_{30}Ag_7$	Pd/Ag ratio approximately unchanged; Pd:Cu approximately 2:1	0.62
$Pd_{70}Cu_{24}Ag_6$	Pd/Ag ratio approximately unchanged; Pd:Cu approximately 3:1	0.58
Optimized EA-PdCuAg NPs	Optimized composition and activation	3.15

Table S5. MA, ECSA, and SA of PdCuAg catalysts after different electrochemical activation cycle numbers.

Activation cycles	MA（A mg_{Pd}^{-1}）	ECSA（m^2 g_{Pd}^{-1}）	SA（mA cm^{-2}）
0	0.54	15.17	3.56
5	2.25	28.54	7.88
10	2.58	31.78	8.12
15	3.12	32.63	9.56
20	3.15	32.77	9.61
50	3.15	32.91	9.57

Table S6. Tafel slope, exchange current density, apparent charge-transfer coefficient, onset potential, and overpotential of EA-PdCuAg NPs and reference catalysts for FAOR.

Catalyst	Tafel slope (mV dec^{-1})	Exchange current density (mA cm^{-2})	Apparent charge-transfer coefficient (α)	Onset potential (mV)	Overpotential (mV)
EA-PdCuAg	173	0.41	0.17	-13	237
EA-PdAg	179	0.37	0.16	-9	241
EA-PdCu	186	0.37	0.15	10	260
EA-Pd	182	0.40	0.16	-6	244
Commercial Pd/C	262	0.37	0.11	5	255

Table S7. MA values of EA-PdCuAg NPs and commercial Pd/C after CA durability tests.

Catalyst	CA time (s)	MA (A mg_{Pd}^{-1})	Retention (%)
EA-PdCuAg	3600	3.13	99.4
EA-PdCuAg	7200	3.06	97.1
EA-PdCuAg	10800	2.79	88.6
EA-PdCuAg	14400	2.54	80.6
Commercial Pd/C	3600	0.14	30.4

Table S8. MA values of EA-PdCuAg NPs and commercial Pd/C after ADT cycling.

Catalyst	ADT cycles	MA (A mg_{Pd}^{-1})	Retention (%)
EA-PdCuAg	2000	3.14	99.7
EA-PdCuAg	4000	3.09	98.1
EA-PdCuAg	6000	2.95	93.7
EA-PdCuAg	8000	2.86	90.8
EA-PdCuAg	10000	2.45	77.8
Commercial Pd/C	200	0.007	1.5

Table S9. ICP-OES composition of EA-PdCuAg NPs after stability testing.

Sample	Pd (atom %)	Cu (atom %)	Ag (atom %)
EA-PdCuAg NPs	70.41	23.04	6.55

Note: The post-stability composition further indicates that the ternary alloy composition is largely retained after electrochemical operation.

Reference

1 T. Shen, S. Chen, R. Zeng, M. Gong, T. Zhao, Y. Lu, X. Liu, D. Xiao, Y. Yang, J. Hu, D. Wang, H. L. Xin and H. D. Abruña, *ACS Catalysis*, 2020, **10,** 9977-9985.

2 H. Cheng, J. Zhou, H. Xie, S. Zhang, J. Zhang, S. Sun, P. Luo, M. Lin, S. Wang, Z. Pan, J. Wang, X. J. Loh and Z. Liu, *Adv. Energy Mater.*, 2023, **13**, 2203893.

3 J. Ding, Z. Liu, X. Liu, B. Liu, J. Liu, Y. Deng, X. Han, W. Hu and C. Zhong, *Angew. Chem. Int. Ed.*, 2020, **59**, 5092-5101.

4 W. C. Wang, T. O. He, X. L. Yang, Y. M. Liu, C. Q. Wang, J. Li, A. D. Xiao, K. Zhang, X. T. Shi and M. S. Jin, *Nano Lett.*, 2021, **21**, 3458-3464.

5 L. Y. Zhang, F. Q. Wang, S. Wang, H. W. Huang, X. M. Meng, Y. R. Ouyang, W. Y. Yuan, C. X. Guo and C. M. Li, *Adv. Funct. Mater.*, 2020, **30**, 9.

6 J. Ding, Z. Liu, X. Liu, J. Liu, Y. Deng, X. Han, C. Zhong and W. Hu, *Adv. Energy Mater.*, 2019, **9**, 1900955.

7 X. Li, Y. M. Liu, J. J. Zhang, B. Yan, C. Q. Jin, J. J. Dou, M. Y. Li, X. H. Feng and G. Liu, *Chem. Mater.*, 2022, **34**, 1385-1391.

8 L. Liang, M. Li, B. Zhang, J. Liang, B. Zeng, L. Wang, Y. Tang, G. Fu and Z. Cui, *Adv. Energy Mater.*, 2023, **13**, 2203803.

9 T. J. Wang, Y. C. Jiang, J. W. He, F. M. Li, Y. Ding, P. Chen and Y. Chen, *Carbon Energy*, 2022, **4**, 283-293.

10 F. Lv, B. Huang, J. Feng, W. Zhang, K. Wang, N. Li, J. Zhou, P. Zhou, W. Yang, Y. Du, D. Su and S. Guo, *Natl. Sci. Rev.*, 2021, **8**, nwab019.

11 X. Zhao, C. Liang, X. Hou, N. Gao, T. Chen, H. Lu, B. Huang and W. Ding, *ACS Sustainable Chem. Eng.*, 2025, **13**, 5624-5632.

12 W. Lu, T. Du, S. Jia, J. Liu, X. Lin, H. Cui, X. Zhang and F. Yang, *Small*, 2025, **21**, 12.

13 Y. W. Hu, Y. Liu, Y. L. Min, Q. J. Xu, K. Jiang and Q. X. Li, *Int. J. Hydrogen Energ*, 2025, **118**, 217-226.

14 Y. M. Ma, Y. H. Li, P. W. Li and Q. X. Li, *Int. J. Electrochem. Sci.*, 2019, **14**, 743-754.

15 C. Rettenmaier, R. M. Arán-Ais, J. Timoshenko, R. Rizo, H. S. Jeon, S. Kühl, S. W. Chee, A. Bergmann and B. Roldan Cuenya, *ACS Catal.*, 2020, **10**, 14540-14551.